THE JOURNAL OF PHYSICAL CHEMISTRY C

Article

Cite This: J. Phys. Chem. C 2019, 123, 8851−8858

pubs.acs.org/JPCC

Electronic Structure of $LiCoO_2$ Surfaces and Effect of Al Substitution

Liang Hong,*,† Linhua Hu,‡ John W. Freeland,§ Jordi Cabana,‡ Serdar Öğüt,† and Robert F. Klie†

†Department of Physics and ‡Department of Chemistry, University of Illinois at Chicago, Chicago, Illinois 60607, United States

§X-ray Science Division, Argonne National Laboratory, Argonne, Illinois 60439, United States

Supporting Information

ABSTRACT: The surface properties of $LiCoO_2$ nanoplatelets, and their chemical modifications with Al^{3+}, were studied using combined experimental and theoretical approaches. Our model shows that the electronic structures of several $LiCoO_2$ surface facets are significantly different from those of bulk $LiCoO_2$, due to altered spin states of surface Co^{3+} atoms. O *K*-edge X-ray absorption revealed a prominent splitting of the Co 3*d*−O 2*p* states, which is attributed to the presence of intermediate-state and/or high-spin-state Co^{3+} at the surface. In particular, the nonpolar (104) surface with intermediate-spin-state Co^{3+} exhibits a strong two-dimensional character of splitting in these states, whereas the polar (001) surface with low-spin-state Co^{3+} has a similar electronic structure to bulk $LiCoO_2$. Partial substitution of Co^{3+} by Al^{3+} through the formation of core−shell architectures increases the ratio of low-spin-state Co^{3+}, resulting in a distinct change in the intensity ratio of the split Co 3*d*−O 2*p* states, as revealed by spectroscopy.

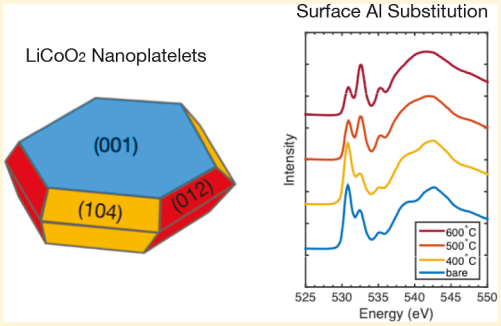

INTRODUCTION

Despite being the most widely used cathode material for Li-ion batteries, lithium cobalt oxide ($LiCoO_2$) undergoes destabilization of its interfaces with the electrolyte upon Li deintercalation. This interfacial instability has been attributed to the oxidized electroactive transition metals present at the surface of subsequently charged electrode.[1] Core−shell nanocrystal heterostructures offer opportunities for improving the stability and functionality of the electrode by introducing inactive ions that passivate the electrode against reaction with the electrolyte. This ability has been recently demonstrated with the compositional and structural tailoring of passivating layers based on aluminum onto $LiCoO_2$ nanoplatelets,[2] fully leveraging tools to manipulate material assembly provided by modern nanotechnology. Through synthetic control, the surface is found to form a $LiAl_xCo_{1-x}O_2$ gradient structure composed of an Al-rich outer layer on a Co-rich core. The resulting heterostructures[2] presented a significant improvement in electrochemical performance and electrode−electrolyte interface stabilization, compared to bare $LiCoO_2$ nanoparticles.[3,4]

It is well established that the physical properties, e.g., lattice parameters and magnetic susceptibility, of $LiCoO_2$ nanocrystals significantly differ from those of bulk $LiCoO_2$ due to surface effects.[5] The surface energies of bare $LiCoO_2$ nanoplatelets were previously studied using first-principles density functional theory (DFT) calculations by Kramer and Ceder.[6] The nanoplatelet was predicted to consist of several low-index surfaces, including (001), (104), (012), and (110) surfaces. Furthermore, Qian *et al.*[7] reported an electronic spin-state transition occurring on the $LiCoO_2$ nanoplatelet surfaces, where intermediate- and high-spin-state (IS and HS) Co^{3+} ions were predicted at (104) and (110) surfaces, respectively, in contrast to the low-spin-state (LS) Co^{3+} observed in bulk $LiCoO_2$. The authors also showed that surface energies computed by DFT could be significantly lowered when the Co^{3+} electronic spin state at (104) and (110) surfaces changed from LS to IS and HS, respectively. This effect of Co spin states on surface energies has been further validated by experiments.[8] Previously, a prominent splitting of the Co 3*d* and O 2*p* states was observed in the X-ray absorption spectra of $LiCoO_2$ nanocrystals of approximately 70 nm in size.[9] The splitting was attributed to the different electronic structures of Co and O at the surface compared to the bulk. A similar observation has been reported for Ti-doped $LiNi_{1-x-y}Mn_xCo_yO_2$ cathode materials and was attributed to a surface effect.[10] However, a fundamental understanding of such a splitting has not yet been provided. Moreover, the atomic and electronic structures of the Al-substituted $LiCoO_2$ surfaces, which are critical to achieving precise control of the physical and electrochemical properties of the nanoelectrode with the desired functionality, are yet to be characterized and understood.[11]

In this work, we perform a combined experimental and theoretical study to address the structural and electronic properties of the bare and Al-substituted $LiCoO_2$ surfaces, using scanning transmission electron microscopy, X-ray diffraction, X-ray absorption spectroscopy, electron energy-loss spectroscopy, and first-principles DFT modeling approaches. O *K*-edge X-ray absorption spectroscopy reveals a

Received: December 4, 2018
Revised: February 25, 2019
Published: March 18, 2019

DOI: 10.1021/acs.jpcc.8b11661
J. Phys. Chem. C 2019, 123, 8851−8858

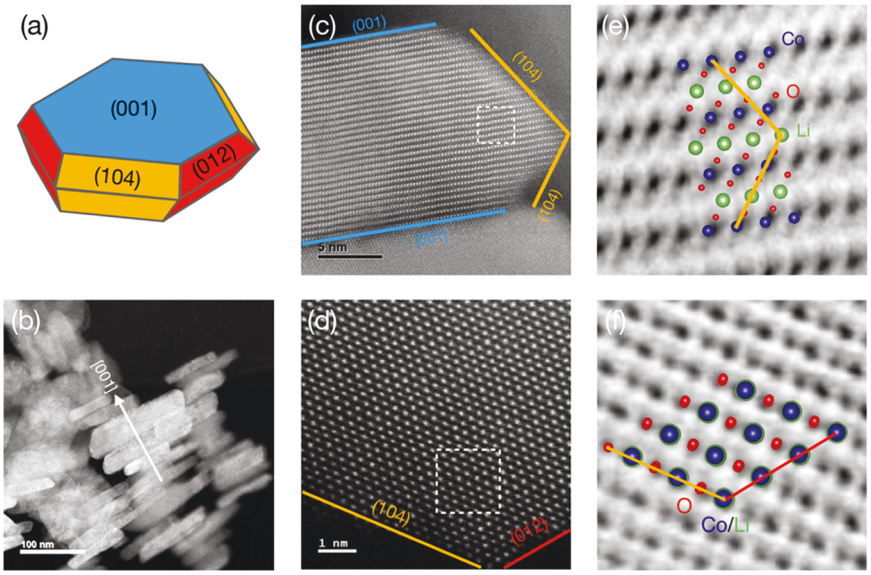

Figure 1. (a) Representative shape of a $LiCoO_2$ nanoplatelet with (001), (104), and (012) surfaces represented by blue, yellow, and red colors, respectively. (b) STEM-LAADF image at low magnification. (c) Atomic-resolution STEM-HAADF image along [010] with (001) and (104) surfaces marked. (d) Atomic-resolution STEM-HAADF image along $[42\bar{1}]$ with (104) and (012) surfaces marked. (e) Atomic-resolution STEM-ABF image taken from the dashed square area in (c). The DFT-optimized structure along [010] is illustrated as the inset with (104) surface marked. (f) Atomic-resolution STEM-ABF image taken from the dashed square area in (d). The DFT-optimized structure along $[42\bar{1}]$ is illustrated as the inset with (104) and (012) surfaces marked. The Li, Co, and O atoms are represented by green, indigo, and red balls, respectively.

prominent splitting of the Co 3*d*−O 2*p* hybridized states resulting from the surface IS and/or HS Co^{3+}. The (104) surface with IS state Co^{3+}, which exhibits a strong in-plane feature of splitting in the hybridized Co 3*d*−O 2*p* states, plays a predominant role in the electronic structure of $LiCoO_2$ nanoplatelets. Furthermore, Al substitution on the $LiCoO_2$ nanoplatelets reduces the surface Co^{3+} IS/LS ratio, resulting in the intensity change of O *K* pre-edge peaks. These results establish a fundamental understanding of the structure−property relationship in $LiCoO_2$ nanoplatelets and advance our ability to precisely tailor the surface properties to enhance the optimized stability and performance of the electrode material in Li-ion batteries.

■ METHODS

Experimental. The $LiCoO_2$ nanoplatelet samples were synthesized using a hydrothermal process, followed by thermal annealing, as introduced in ref 2. Three samples were used for experiments in this work: (1) bare $LiCoO_2$ nanoplatelets, marked as bare; (2) surface-modified $LiCoO_2$ nanoplatelets with a theoretical surface Al/Co ratio of 2%, marked as 1Al; (3) surface-modified $LiCoO_2$ nanoplatelets with a theoretical surface Al/Co ratio of 6%, marked as 3Al. The details of sample synthesis are presented in the Supporting Information.

The scanning transmission electron microscopy (STEM) images and electron energy-loss (EEL) spectra were obtained using the aberration-corrected JEOL JEM-ARM200CF microscope operating at an acceleration voltage of 200 kV, which allows a 78 pm spatial resolution and a 0.35 eV energy resolution.[12] The high-angle annular dark-field (HAADF), low-angle annular dark-field (LAADF), and annular bright-field (ABF) images were acquired using a convergence semi-angle of 23 mrad and a collection angle from 90 to 175 mrad for HAADF imaging, 40 to 90 mrad for LAADF imaging, and 11 to 23 mrad for ABF imaging. EELS was collected using the upgraded Gatan Quantum imaging filter with a convergence angle of 30 mrad and a collection angle with 35 mrad. An energy dispersion of 0.3 eV/channel was used for the measurement of the O *K*-edge spectrum.

Powder X-ray diffraction (XRD) patterns were collected on a Bruker D8 advanced X-ray diffractometer. X-ray absorption spectroscopy (XAS) was conducted at the O *K*-edge and Co *L*-edge at beamline 4-ID-C at the Advanced Photon Source. Samples were loaded into the measurement chamber from an Ar-filled transfer stage, using an Ar-filled glovebag. To examine the electronic properties at materials surface, the spectra were collected utilizing the sample photocurrent for the total electron yield (TEY), which probes the surface of a material at $\sim 10^{-9}$ Torr. Data were obtained at a spectral resolution of 0.2 eV with a 2 s dwell time. Three scans were performed on each sample, at each absorption edge, and scans were averaged to maximize the signal-to-noise ratio. An energy reference for Co and O was recorded simultaneously with the XAS for accurate energy alignment.

Modeling. First-principles density functional theory (DFT) calculations were carried out using the generalized gradient approximation (GGA) with the Hubbard *U* correction (GGA + *U*) method, as implemented in Vienna Ab initio Simulation Package (VASP).[13,14] The GGA + *U* method has been reported to be a robust method for modeling the $LiCoO_2$ system, and the effective *U* value for Co 3*d* electrons was chosen as $U - J = 3.3$ eV in accordance with previous theoretical studies.[6,7] All of the calculations were performed using a plane wave cutoff of 550 eV. Slab models with two symmetric surfaces separated by a vacuum of 20 Å were used to simulate the $LiCoO_2$ surfaces. Monkhorst−Pack *k*-point grids of 8 × 4 × 1 and 16 × 8 × 1 were used for geometry optimization and density of states (DOS) calculations, respectively. Two polar surfaces, (001) and (012), and two nonpolar surfaces, (104), and (110), were considered in this work. For the polar (001) and (012) surfaces, 0.5 monolayer (ML) of Li and O was considered as the terminations,

DOI: 10.1021/acs.jpcc.8b11661
J. Phys. Chem. C 2019, 123, 8851−8858

respectively, to compensate the dipoles in the slabs.[6,15] All of the slabs were therefore stoichiometric with the chemical formula of $(LiCoO_2)_n$. We found that $n = 12$, corresponding to a slab thickness of ~20 Å, is enough to simulate the surface properties. The surface models are shown in the Supporting Information. Core−hole effects were not included in our calculations, as the O *K* pre-edge features have been shown to be better reproduced with the use of Hubbard *U* without core−hole effects in ref 16.

RESULTS AND DISCUSSION

Bare $LiCoO_2$ Nanoplatelets. The bare $LiCoO_2$ sample was characterized using aberration-corrected STEM imaging. The equilibrium shape of $LiCoO_2$ single particle observed from the STEM images, shown in Figure 1a, consists of (001), (104), and (012) surfaces, among which (001) possesses the largest surface area. LAADF images at low magnification, such as the example shown in Figure 1b, reveal that the nanoplatelets favor extended stacking along the [001] direction, which largely reduces the exposed area of (001) surface in the nanoplatelets. The atomic structures of (001), (104), and (012) surfaces in the $LiCoO_2$ nanoplatelet can be directly observed through atomic-resolution HAADF imaging along [010] and $[42\bar{1}]$ zone directions, shown in Figure 1c,d, respectively. The three surfaces are atomically sharp without significant structural changes compared with the bulk area. The atomic structure is further characterized from the near-edge area using atomic-resolution ABF imaging, which enables the observation of O columns, shown in Figure 1e,f. It can be seen that the STEM-resolved $LiCoO_2$ structure is in good agreement with the DFT-optimized structure in terms of the lattice spacing, surface orientation, and elemental arrangement, providing validation for the structural models used in the DFT simulation.

The energy-loss near-edge structure (ELNES) and X-ray absorption near-edge structure (XANES) at the O *K*-edge were measured using EELS in point mode and XAS in TEY mode, respectively, as shown in Figure 2. Similarly, intense signals were observed in both O *K*-edge ELNES and XANES at 537 and 543 eV, which are associated with the hybridization of O 2*p* and Co 4*sp* states, respectively. In contrast, obvious differences were found in pre-edge signals (onset features), at around 531 eV, which originate from the hybridization of O 2*p* and Co 3*d* states. A single pre-edge peak at 531 eV (peak A) was detected in ELNES, whereas the XANES showed two peaks A_1 and A_2 at 530.6 and 532 eV, respectively, with a measured splitting $\Delta = 1.4$ eV. The minor peak, A_3, at 535.2 eV is usually assigned to Li_2CO_3 surface impurities[17] and will not be discussed in detail in this work. The difference between the ELNES and XANES lies in the probing depth; although EELS is a transmission technique, XAS was measured using a photoelectron detector that probes less than 10 nm into the material. Therefore, the results suggest that the electronic structures at the $LiCoO_2$ bulk and surface are significantly different. As demonstrated before, the splitting of the Co 3*d* and O 2*p* states has not been reported in previous XAS studies. We attributed this to the fact that $LiCoO_2$ studies of materials with a large grain size of limited surface areas will not exhibit the effects reported here, which appear to be the results of specific surface terminations and facets. In the following discussion, we will focus on the two split pre-edge peaks, A_1 and A_2, in $LiCoO_2$ nanoplatelets.

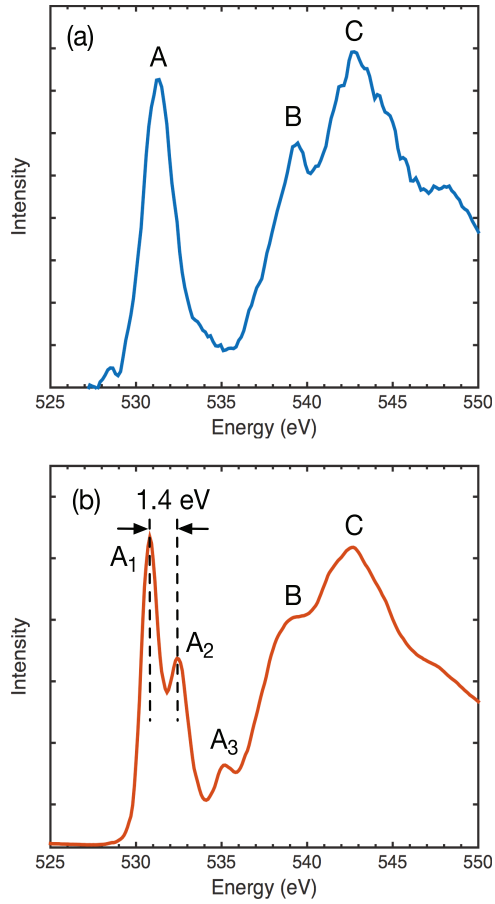

Figure 2. (a) O *K*-edge ELNES for bare $LiCoO_2$ nanoplatelets. Three characteristic peaks are labeled as A, B, and C. (b) O *K*-edge XANES for bare $LiCoO_2$ nanoplatelets. The characteristic peaks are labeled as A_1, A_2, A_3, B, and C.

The DFT-calculated properties for the bare $LiCoO_2$ surfaces are summarized in Table 1. The relative stability of each surface can be indicated by the calculated surface energy, γ. Among all of the investigated surfaces, the nonpolar (104) surface is found to possess the lowest energy. The experimentally dominant (001) surface is the second lowest, but the Li termination means that its energy is notably sensitive to the chemical potential of surface Li^+. More specifically, the surface energy of (001) can decrease significantly from about 1−0.4 J/m^2, as the Li chemical potential is lowered. Similarly, the polar O-terminated (012) surface energy can also be lowered to a value comparable to the (104) surface under O-rich conditions.[6]

Table 1. DFT-Calculated $LiCoO_2$ Surface Properties: Lattice Constants *a* and *b*, Surface Co Coordination, Surface Co^{3+} Spin State, and Surface Energy γ

surface	polarity	*a* (Å)	*b* (Å)	∠*a*, *b* (deg)	Co coord.	spin state	γ (J/m^2)
(001)	polar	2.832	5.663	60.0	6	LS	1.040
(012)	polar	2.832	4.987	90.0	5	IS	1.652
(104)	nonpolar	2.832	6.396	63.7	5	IS	0.791
(110)	nonpolar	4.987	4.904	70.9	4	HS	1.532

According to the calculated density of states (DOS) projected on the Co 3*d* t_{2g} and e_g orbitals, the surface Co

DOI: 10.1021/acs.jpcc.8b11661
J. Phys. Chem. C 2019, 123, 8851−8858

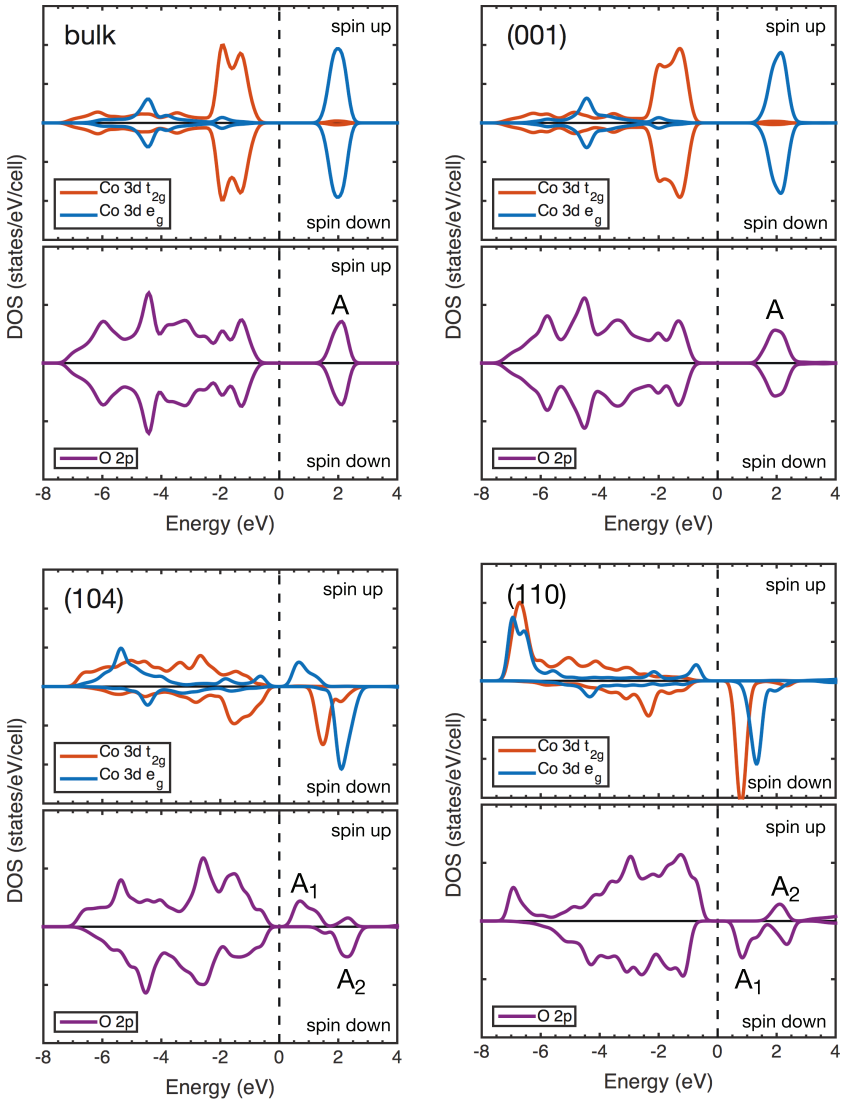

Figure 3. Spin-resolved DOS projected on Co 3*d* and O 2*p* orbitals for the $LiCoO_2$ bulk, (001), (104), and (110) surfaces. The characteristic peaks are marked by A, A_1, and A_2. Fermi energy is shifted to 0 eV.

possesses different spin states on different surfaces due to the changes in the Co coordination. The sixfold coordinated Co^{3+} ions in the polar (001) surface are in the low-spin state (LS, $t_{2g}^6e_g^0$) and the 5-fold Co^{3+} ions in the polar (012) and nonpolar (104) surfaces are in the intermediate-spin state (IS, $t_{2g}^5e_g^1$), whereas the fourfold Co^{3+} ions in the nonpolar (110) surface are in the high-spin state (HS, $t_{2g}^4e_g^2$). The spin-resolved projected DOS on Co 3*d* (t_{2g} and e_g) and O 2*p* orbitals are plotted for bulk $LiCoO_2$, (001), (104), and (110) surfaces in Figure 3. The DOS profile for the polar (001) surface is similar to that of bulk $LiCoO_2$, where the Co t_{2g} orbital is fully occupied, whereas the e_g orbital is empty, lying 2 eV above the Fermi level. The characteristic O peak A at 2 eV above the Fermi level, originating from the hybridization with Co e_g orbitals, corresponds to peak A in the O *K*-edge ELNES. Compared with the DOS in the bulk, the unoccupied Co e_g orbital in the (104) surface splits into two components at 0.8 eV (spin up) and 2.3 eV (spin down) above the Fermi level due to the partial occupancy of the e_g orbital. Accordingly, the unoccupied O 2*p* states, A_1 at 0.8 eV and A_2 at 2.3 eV, can be attributed to the hybridization with the Co unoccupied e_g split states. The DOS profile for the (012) surface with IS Co^{3+} exhibits similar features as that for the (104) surface (shown in the Supporting Information). In the DOS of (110) surface with HS Co^{3+}, the unoccupied O 2*p* states A_1 at 0.8 eV can be attributed to the hybridization with the unoccupied Co t_{2g} states at 0.8 eV above the Fermi level, whereas the A_2 peak at 2.3 eV stems from the antibonding states with Co underneath the surface. These two distinct O states, A_1 and A_2, found in the (104), (012), and (110) surfaces from the DFT modeling reproduce the experimentally observed peak splitting in O *K*-edge XANES. Indeed, the splitting energies from the DFT modeling (ΔE = 1.5 eV) and the XAS (Δ = 1.4 eV) are in good agreement. Similar splitting behavior at the O pre-edge has been reported in $Ca_3Co_4O_9$ thin films with HS Co^{4+}.[18] It further appears that the Co L_3/L_2-ration is not a good measure for the Co^{3+} spin state, whereas the O *K*-edge pre-peak has previously been used to quantify the Co-ion spin state, for example, in $LaCoO_3$.[19]

To further explore the O *K*-edge splitting, the orbital-projected DOS for the O atoms at the (104) surface, which has the lowest surface energy, is illustrated with the surface model in Figure 4. As mentioned above, the surface fivefold Co^{3+} ion is in an IS state, whereas the sixfold Co^{3+} ions underneath the

DOI: 10.1021/acs.jpcc.8b11661
J. Phys. Chem. C 2019, 123, 8851−8858

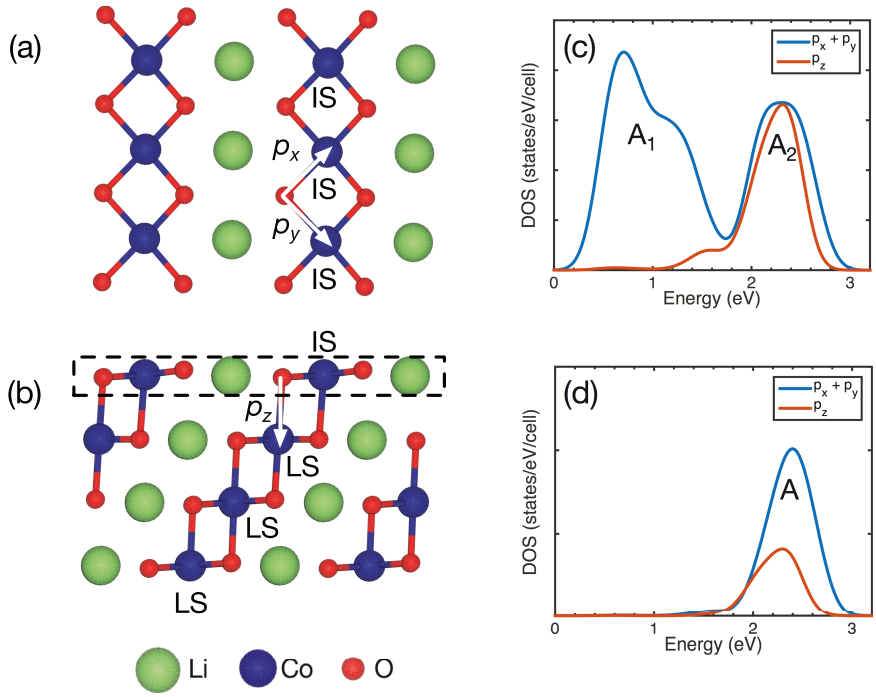

Figure 4. (a) Top view of the $LiCoO_2$ (104) surface structure with IS Co^{3+}. The directions of O p_x and p_y states are marked by white arrows. (b) Side view of the $LiCoO_2$ (104) surface structure with IS and LS Co^{3+} in different layers. The direction of O p_z state is marked by a white arrow and the surface layer is marked by the dashed rectangles. (c) DOS (summed spin-up and spin-down states) of in-plane ($p_x + p_y$) and out-of-plane (p_z) O unoccupied states from the surface layer. The split peaks from in-plane states are marked by A_1 and A_2. (d) DOS (summed spin-up and spin-down states) of in-plane ($p_x + p_y$) and out-of-plane (p_z) O unoccupied states from the layer underneath the surface. The peak from in-plane states is marked by A. Fermi energy is shifted to 0 eV.

surface are in an LS state. The splitting is only observed in the O p_x and p_y states (peaks A_1 and A_2 in Figure 4b) from the surface layer, stemming from the in-plane IS Co−O bonding, which has a strong two-dimensional character. On the other hand, the O p_z states, stemming from the out-of-plane LS Co−O bonding, only contribute to peak A_2. In addition to the (104) surface, the (012) surface with IS Co^{3+} and (110) surface with HS Co^{3+} also contribute to the splitting of O pre-edge, in accordance with the analysis discussed previously. Consequently, the pre-edge splitting is ascribed to the presence of surface IS and/or HS Co^{3+}, and the intensity of peak A_1 can be employed to directly assess the amount of surface IS and/or HS Co^{3+}. This conclusion serves to rationalize the observation of pre-edge splitting in the O *K*-edge XANES of $LiCoO_2$ nanoplatelets, which possess larger surface areas than bulk $LiCoO_2$ materials previously measured in the literature.[20,21]

Effects of Al Substitution on the $LiCoO_2$ Surface. The effects of the substitution of Co by Al on the $LiCoO_2$ surface properties were studied using core−shell heterostructures based on $LiCoO_2$ nanoplatelets modified with conformal Al-rich layers, where the compositional gradient into the interior, from a pure aluminum oxide layer to $LiAl_xCo_{1-x}O_2$ solid solutions, can be controlled by changing the annealing temperature.[2] Figure 5 shows the XRD patterns for the two Al-substituted $LiCoO_2$ samples (1Al and 3Al) and the bare $LiCoO_2$ at different temperatures. The peaks shown in the bare sample correspond to the layered structure of the high-temperature form of $LiCoO_2$, as demonstrated by the splitting of the (006)/(012) and (108)/(110) peaks,[3,22] without any visible impurities. This layered structure is preserved, in all cases, after the introduction of Al into the sample. The magnified view of the (003) reflection reveals a gradual shift to

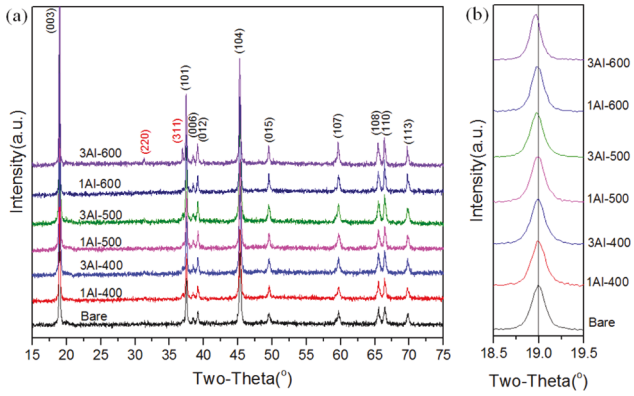

Figure 5. (a) XRD patterns of $LiCoO_2$ nanocrystal heterostructures. The bare sample was calcined at 500 °C for 3 h. Other samples were fabricated by modifying the surface of the bare $LiCoO_2$ nanoplatelets with different Al concentrations (1Al, 3Al) and thermal treatments (400, 500, and 600 °C) for 3 h. Miller indices (003), (101), (006), (012), (104), (015), (107), (108), (110), and (113) correspond to $LiCoO_2$, whereas (220) and (311) correspond to Co_3O_4. (b) Zoom between 18.5 and 19.5°.

lower angles for 3Al as the temperature increased from 500 to 600 °C; no shift was observed in any other samples. This observation suggests the introduction of Al on $LiCoO_2$ as a discrete aluminum oxide film at 400 °C, but this oxide subsequently reacts with $LiCoO_2$, forming $LiAl_xCo_{1-x}O_2$ and Co_3O_4 upon further heating, as indicated by the distinct (220) and (311) peaks of the latter in 3Al made at 600 °C.[2]

Figure 6 shows the O *K*-edge XANES for the 1Al and 3Al samples at different annealing temperatures. Both 1Al and 3Al samples at 400 °C show the peaks with a similar intensity

DOI: 10.1021/acs.jpcc.8b11661
J. Phys. Chem. C 2019, 123, 8851−8858

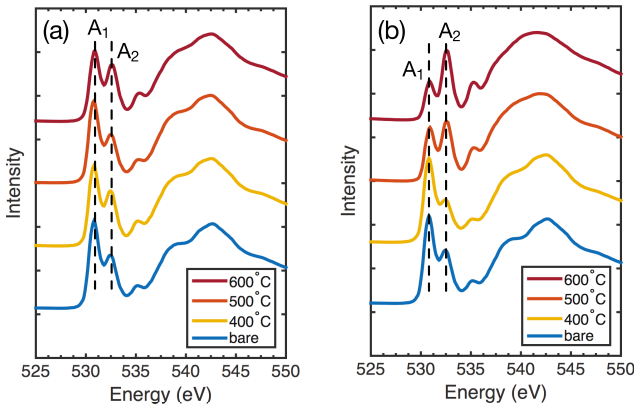

Figure 6. O *K*-edge XANES of $LiCoO_2$ nanocrystal heterostructures, (a) 1Al and (b) 3Al, at temperatures of 400, 500, and 600 °C. Data for bare $LiCoO_2$ is shown for comparison. The split pre-edge peaks are marked as A_1 and A_2.

profile compared with the bare $LiCoO_2$, suggesting that the local chemical environment of Co at the surface does not change with the presence of Al at 400 °C, as would be expected from an $Al_2O_3/LiCoO_2$. As the annealing temperature increased to 600 °C, $LiAl_xCo_{1-x}O_2$ gradients were introduced. For the 1Al sample, the intensity of peak A_1 slightly decreases, whereas that of peak A_2 slightly increases. This trend is significantly more pronounced for the 3Al sample, where the A_1/A_2 intensity ratio even reverses at the highest temperature. This change suggests that the Al concentration has a significant effect on the electronic structure of the $LiAl_xCo_{1-x}O_2$ surface. Co L_3- and L_2-edge XANES were also measured for the samples to assess whether the Co valence state was affected by the annealing process, as well. However, no visible peak shift or intensity change can be observed compared with the bare $LiCoO_2$ (Figure 7). Therefore, the surface Co valence remains +3, as indicated by the L_3/L_2 intensity ratio, as Al^{3+} is introduced in the surface of the transition-metal oxide.

The $LiAl_xCo_{1-x}O_2$ surfaces were simulated by replacing the surface Co with Al atoms in the extended 2 × 2 surface cell with Al concentrations x = 0.5 and 0.25. In the optimized surface structures (shown in the Supporting Information), the differences between Al−O and Co−O bond lengths are found

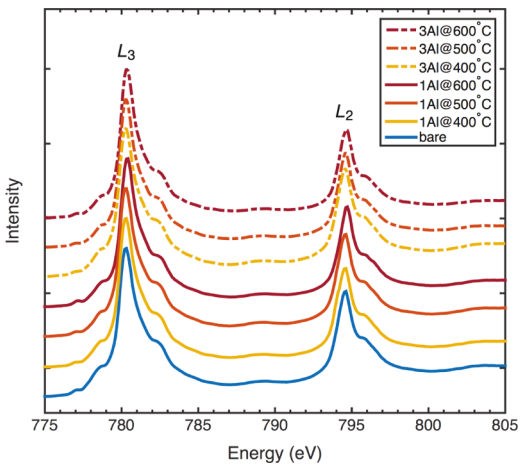

Figure 7. Co $L_{3,2}$-edge XANES for bare $LiCoO_2$, 1Al and 3Al, at different temperatures.

to be less than 0.05 Å, and no significant surface reconstruction is observed. As shown in Table 2, the surface energy of the Al-

Table 2. DFT-Calculated $LiAl_xCo_{1-x}O_2$ (x = 0.5, 0.25) Surface Properties: Surface Co^{3+} Spin State, Surface Energy γ, and Surface Energy Difference $\Delta\gamma$ between Al-Substituted and Bare $LiCoO_2$

surface	x	spin state	γ (J/m^2)	$\Delta\gamma$ (J/m^2)
(001)	0.5	LS	1.049	0.010
(001)	0.25	LS	1.035	−0.005
(104)	0.5	IS	0.760	−0.032
(104)	0.25	IS	0.764	−0.027
(012)	0.5	IS	1.805	0.153
(110)	0.5	HS	1.702	0.169

substituted (001) surface barely changes, whereas that of the Al-substituted (104) surface slightly lowers. The surface energy of (012) and (110) increases after Al substitution at x = 0.5, suggesting that the (012) and (110) surfaces might be less favorable for this chemical substitution than the (001) and (104) surfaces.

The effect of Al substitution on the surface electronic structure is further explored through the DOS projected on O unoccupied 2p orbitals for the (104) surface, as shown in Figure 8. In both Al-substituted cases, compared with the bare

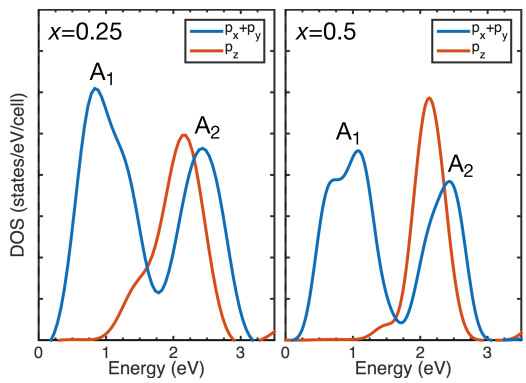

Figure 8. DOS (summed spin-up and spin-down states) of in-plane ($p_x + p_y$) and out-of-plane (p_z) O unoccupied states at $LiAl_xCo_{1-x}O_2$ (104) surfaces, where x = 0.25 and 0.5. The split peaks from in-plane states are marked by A_1 and A_2. Fermi energy is shifted to 0 eV.

$LiCoO_2$ (104) surface, the in-plane O 2p states ($p_x + p_y$) remain split into two peaks A_1 and A_2 above the Fermi level, whereas the out-of-plane O 2p states (p_z) slightly shift to lower energy due to the tilting of the out-of-plane Co−O bonds. As the Al concentration x increases from 0.25 to 0.5, the intensities of both A_1 and A_2 peaks reduce compared to that of the out-of-plane states, since the number of the in-plane IS Co−O bonds reduces as more surface IS Co is substituted by Al, whereas the number of the out-of-plane LS Co−O remains the same. Furthermore, the effect of Al substitution of LS Co is also examined in the layers underneath the (104) surface as well as in the (001) surface. No significant change is found in the DOS of O 2p orbitals after Al substitution except the decreased intensity of the single peak A (shown in the Supporting Information). Therefore, the experimentally observed decrease in the A_1/A_2 intensity ratio as the Al concentration increases in the form of a $LiAl_xCo_{1-x}O_2$ solid solution at higher temperature can be attributed to the

DOI: 10.1021/acs.jpcc.8b11661
J. Phys. Chem. C 2019, 123, 8851−8858

decreased surface Co^{3+} IS/LS ratio. In the case of 3Al sample at 600 °C, the intensity of peak A_1 is significantly suppressed, whereas the intensity of peak A_2 increases accordingly, as more LS Co^{3+} dominates the surface.

■ CONCLUSIONS

Combining experimental and theoretical results, we observe that the $LiCoO_2$ nanoplatelet mainly consists of atomically sharp (001), (104), and (012) surfaces, which have electronic properties that, in the case of the latter two facets, deviate from bulk $LiCoO_2$. From the comparison of O *K*-edge EELS and, especially, XAS, we uncover the existence of splitting of signals at the pre-edge due to surface effects. DFT simulation results indicate that the splitting originates from the existence of IS and/or HS Co^{3+} at different surface facets due to altered Co coordinations from the ideal octahedron. From the projected DOS of Co and O at the (104) surface, which is predicted to be lowest in energy, we find that the splitting of the Co 3*d*−O 2*p* hybridized states is induced by the in-plane IS Co−O bonding with a strong two-dimensional character. Therefore, the existence of splitting directly reflects the amount of surface IS and/or HS Co^{3+}. Substitution of Co^{3+} by Al^{3+} on the surface of the $LiCoO_2$ nanoplatelets, through core−shell structures with compositional gradients, did not affect the Co valence; yet, the intensity ratio of O pre-edge reverted as the Al concentration increased, and DFT modeling indicated that Al substitution reduced the surface IS/LS ratio, explaining the changes in intensity ratio. Our work illustrates that the electronic properties of $LiCoO_2$ surfaces can be tailored by controlling crystal growth and chemical compositions at the atomic level, providing the opportunities for designing and developing novel Li-ion battery materials with higher stability and better performance.

■ ASSOCIATED CONTENT

Supporting Information

The Supporting Information is available free of charge on the ACS Publications website at DOI: 10.1021/acs.jpcc.8b11661.

(1) Synthesis method; (2) DFT models for simulating the (001), (104), (012), and (110) surfaces (Figure S1); (3) Calculation method of surface energies; (4) Projected DOS for the $LiCoO_2$ (012) surface (Figure S2); (5) DFT-optimized structures for Al-substituted $LiCoO_2$ (104) surfaces (Figure S3); (6) Projected DOS for Al-substituted $LiCoO_2$ (001) surfaces (Figure S4) (PDF)

■ AUTHOR INFORMATION

Corresponding Author

*E-mail: ikiddo1412@gmail.com. Phone: +1 (312)-888-6350.

ORCID

Liang Hong: 0000-0003-1499-5806
Linhua Hu: 0000-0002-0177-3983
Jordi Cabana: 0000-0002-2353-5986

Notes

The authors declare no competing financial interest.

■ ACKNOWLEDGMENTS

Synthesis and X-ray analysis by L.H.H. and J.C. were supported by the National Science Foundation under Grant No. CBET-1605126. DFT modeling and STEM/EELS characterization by L.H., S.O., and R.F.K. were supported by the National Science Foundation DMR Ceramics program under Grant No. NSF-1831406. Use of the Advanced Photon Source was supported by the US Department of Energy, Office of Science, under contract No. DE-AC02-06CH11357. Acquisition of JEOL JEM-ARM200CF was supported by an MRI-R^2 grant from the National Science Foundation (DMR-0959470). The Gatan Quantum GIF acquisition at UIC was supported by an MRI grant from the National Science Foundation (DMR-1626065). The authors acknowledge the use of the Electron Microscopy Service and the High-Performance Computing Service at the University of Illinois at Chicago. The authors thank Dr. Hakim Iddir and Dr. Juan Garcia for useful discussions and suggestions.

■ REFERENCES

(1) Alva, G.; Kim, C.; Yi, T.; Cook, J. B.; Xu, L.; Nolis, G. M.; Cabana, J. Surface chemistry consequences of Mg-based coatings on $LiNi_{0.5}Mn_{1.5}O_4$ electrode materials upon operation at high voltage. *J. Phys. Chem. C* **2014**, *118*, 10596−10605.

(2) Hu, L.; Bruner, P.; Grehl, T.; Brongersma, H. H.; Cabana, J. Control of chemical structure in core-shell nanocrystals for the stabilization of battery electrode/electrolyte interfaces. *Chem. Mater.* **2017**, *29*, 5896−5905.

(3) Okubo, M.; Hosono, E.; Kim, J.; Enomoto, M.; Kojima, N.; Kudo, T.; Zhou, H.; Honma, I. Nanosize effect on high-rate Li-ion intercalation in $LiCoO_2$ electrode. *J. Am. Chem. Soc.* **2007**, *129*, 7444−7452.

(4) Chen, H.; Grey, C. P. Molten salt synthesis and high rate performance of the "desert-rose" form of $LiCoO_2$. *Adv. Mater.* **2008**, *20*, 2206−2210.

(5) Okubo, M.; Kim, J.; Kudo, T.; Zhou, H.; Honma, I. Anisotropic surface effect on electronic structures and electrochemical properties of $LiCoO_2$. *J. Phys. Chem. C* **2009**, *113*, 15337−15342.

(6) Kramer, D.; Ceder, G. Tailoring the morphology of $LiCoO_2$: A first principles study. *Chem. Mater.* **2009**, *21*, 3799−3809.

(7) Qian, D.; Hinuma, Y.; Chen, H.; Du, L.-S.; Carroll, K. J.; Ceder, G.; Grey, C. P.; Meng, Y. S. Electronic spin transition in nanosize stoichiometric lithium cobalt oxide. *J. Am. Chem. Soc.* **2012**, *134*, 6096−6099.

(8) Maram, P. S.; Costa, G. C.; Navrotsky, A. Experimental confirmation of low surface energy in $LiCoO_2$ and implications for lithium battery electrodes. *Angew. Chem., Int. Ed.* **2013**, *52*, 12139−12142.

(9) Kwon, B. J.; Phillips, P. J.; Key, B.; Dogan, F.; Freeland, J. W.; Kim, C.; Klie, R. F.; Cabana, J. Nanocrystal heterostructures of $LiCoO_2$ with conformal passivating shells. *Nanoscale* **2018**, *10*, 6954−6961.

(10) Lin, F.; Nordlund, D.; Pan, T.; Markus, I. M.; Weng, T.-C.; Xin, H. L.; Doeff, M. M. Influence of synthesis conditions on the surface passivation and electrochemical behavior of layered cathode materials. *J. Mater. Chem. A* **2014**, *2*, 19833−19840.

(11) Cabana, J.; Kwon, B. J.; Hu, L. Mechanisms of degradation and strategies for the stabilization of cathode-electrolyte interfaces in Li-ion batteries. *Acc. Chem. Res.* **2018**, *51*, 299−308.

(12) Klie, R.; Gulec, A.; Guo, Z.; Paulauskas, T.; Qiao, Q.; Tao, R.; Wang, C.; Low, K.; Nicholls, A.; Phillips, P. The new JEOL JEM-ARM200CF at the University of Illinois at Chicago. *Cryst. Res. Technol.* **2014**, *49*, 653−662.

(13) Kresse, G.; Furthmüller, J. Efficient iterative schemes for ab initio total-energy calculations using a plane-wave basis set. *Phys. Rev. B* **1996**, *54*, 11169.

(14) Kresse, G.; Joubert, D. From ultrasoft pseudopotentials to the projector augmented-wave method. *Phys. Rev. B* **1999**, *59*, 1758.

(15) Garcia, J. C.; Bareño, J.; Yan, J.; Chen, G.; Hauser, A.; Croy, J. R.; Iddir, H. Surface structure, morphology, and stability of Li

DOI: 10.1021/acs.jpcc.8b11661
J. Phys. Chem. C 2019, 123, 8851−8858

$(Ni_{1/3}Mn_{1/3}Co_{1/3})O_2$ cathode material. *J. Phys. Chem. C* **2017**, *121*, 8290−8299.

(16) Juhin, A.; De Groot, F.; Vankó, G.; Calandra, M.; Brouder, C. Angular dependence of core hole screening in LiCoO 2: A DFT+ *U* calculation of the oxygen and cobalt *K*-edge x-ray absorption spectra. *Phys. Rev. B* **2010**, *81*, No. 115115.

(17) Yogi, C.; Takamatsu, D.; Yamanaka, K.; Arai, H.; Uchimoto, Y.; Kojima, K.; Watanabe, I.; Ohta, T.; Ogumi, Z. Soft X-ray absorption spectroscopic studies with different probing depths: Effect of an electrolyte additive on electrode surfaces. *J. Power Sources* **2014**, *248*, 994−999.

(18) Klie, R. F.; Qiao, Q.; Paulauskas, T.; Gulec, A.; Rebola, A.; Öğüt, S.; Prange, M. P.; Idrobo, J.; Pantelides, S. T.; Kolesnik, S.; et al. Observations of Co^{4+} in a higher spin state and the increase in the seebeck coefficient of thermoelectric $Ca^3Co^4O^9$. *Phys. Rev. Lett.* **2012**, *108*, No. 196601.

(19) Klie, R.; Zheng, J.; Zhu, Y.; Varela, M.; Wu, J.; Leighton, C. Direct measurement of the low-temperature spin-state transition in $LaCoO_3$. *Phys. Rev. Lett.* **2007**, *99*, No. 047203.

(20) Yoon, W.-S.; Kim, K.-B.; Kim, M.-G.; Lee, M.-K.; Shin, H.-J.; Lee, J.-M.; Lee, J.-S.; Yo, C.-H. Oxygen contribution on Li-ion intercalation-deintercalation in $LiCoO_2$ investigated by O *K*-edge and Co *L*-edge X-ray absorption spectroscopy. *J. Phys. Chem. B* **2002**, *106*, 2526−2532.

(21) Graetz, J.; Hightower, A.; Ahn, C.; Yazami, R.; Rez, P.; Fultz, B. Electronic structure of chemically-delithiated $LiCoO_2$ studied by electron energy-loss spectrometry. *J. Phys. Chem. B* **2002**, *106*, 1286−1289.

(22) Li, C.-N.; Yang, J.-M.; Krasnov, V.; Arias, J.; Nieh, K.-W. Phase transformation of nanocrystalline $LiCoO_2$ cathode after high-temperature cycling. *Electrochem. Solid-State Lett.* **2008**, *11*, A81−A83.

DOI: 10.1021/acs.jpcc.8b11661
J. Phys. Chem. C 2019, 123, 8851−8858